

Effect of cathodic hydrogen-charging current density on mechanical properties of prestrained high strength steels

Xinfeng Li ^a, Jin Zhang ^b, Yanfei Wang ^c, Bo Li ^a, Peng Zhang ^a, Xiaolong Song ^{a,*}

^a State Key Laboratory for Mechanical Behavior of Materials, School of Materials Science and Engineering, Xi'an Jiaotong University, Xi'an 710049, China

^b Department of Geosciences, Center for Materials by Design, and Institute for Advanced Computational Science, State University of New York, Stony Brook, NY 11794-2100, USA

^c School of Chemical Engineering & Technology, China University of Mining and Technology, Xuzhou 221116, China



ARTICLE INFO

Article history:

Received 27 January 2015

Received in revised form

19 May 2015

Accepted 1 June 2015

Available online 3 June 2015

Keywords:

Hydrogen embrittlement

High strength steel

Prestrain

Tensile property

ABSTRACT

The present work investigated the effect of cathodic hydrogen-charging current density on mechanical properties of prestrained high strength steels. This was done by tensile tests on both hydrogen-charged and -uncharged prestrained specimens at a cross-head displacement speed of 0.03 mm/min. The influence of prestrain on hydrogen behavior was also studied using an electrochemical permeation technique. The results show that the relationship between ultimate tensile strength of the hydrogen-charged specimens (UTS-H) and prestrain depends on current density. The UTS-H decreases with increasing current density independent on prestrain. With an increase in prestrain the diffusion coefficient of hydrogen gradually decreases, which is attributed to increasing dislocations density acted as hydrogen traps. SEM fractograph reveals that hydrogen charging causes a change from ductile to brittle failure.

© 2015 Elsevier B.V. All rights reserved.

1. Introduction

Due to a combination of high strength and excellent toughness, high strength steels have been widely used. However, hydrogen deteriorates the mechanical properties of steels and gives rise to hydrogen embrittlement (HE). Generally the failures caused by HE are invisible and unpredictable, accompanying by catastrophic consequences [1–3]. Moreover, it is well-established that the sensitivity to HE increases with increasing strength level when the strength is over 1 GPa [4,5]. As a consequence, it is necessary to investigate the interaction between hydrogen and high strength steels.

Previous investigations on hydrogen-induced softening/hardening have been focused on various steels and the results are inconclusive. The effect of hydrogen on dislocations motion was either enhancing dislocations mobility [6–8] or pinning dislocations motion [9–11], corresponding to microscopical hydrogen-induced softening and hardening respectively. A study [12] showed that an increase or decrease in flow stress was determined by the competition between the effect of hydrogen on slip localization and on the dislocation mobility. Matsui et al. [13] suggested that hydrogen-induced softening or hardening of high purity iron depended on the temperature. Below 190 K hydrogen increased flow stress

while hydrogen decreased flow stress above 190 K. Numerical simulation results [14] showed that a loss of strength was dependent on the hydrogen content. Two hydrogen atoms placed in crack tip caused 22% drop in strength while further increase in hydrogen atoms had no significant effect on strength loss. In addition, compared with in air, the tensile strength did not change in high pressure hydrogen for various materials, such as 0.028% C Armco iron, 0.22% C normalized, ASTM A-515 Gr 70, AISI 1020 [15,16].

The effect of hydrogen on mechanical properties of prestrained materials had been studied for dual-phase steels [17], 310S stainless steels [18], 2205 duplex stainless steels [19], 304L stainless steels [20] and pure iron [21]. The purpose of the present study is to investigate the effect of cathodic current density on mechanical properties of prestrained high strength steels. The influence of prestrain on hydrogen behavior and the role of hydrogen on fracture behavior are analyzed. Furthermore, the effect of cathodic current density on relationship between ultimate tensile strength of hydrogen-charged specimens (UTS-H) and prestrain is discussed.

2. Experimental method

Screw-thread steel bars were used in this study. The chemical composition is shown in Table 1. After hot-rolled, the steel bars underwent air-cooling to room temperature and then tempering

* Corresponding author. Fax: +86 29 82663453.

E-mail address: songxl@mail.xjtu.edu.cn (X. Song).

Table 1

Chemical composition of the high strength steel (wt%).

Element	C	Si	Mn	P	S	Cr	Ni	Cu	Al	Fe
Analyzed	0.25	1.41	2.19	0.014	0.0049	1.07	0.011	0.018	0.015	Balance

at 623 K for 5 h. The smooth cylindrical specimens with dimensions 5 mm diameter × 25 mm length were machined from the bars with axial direction paralleling to the rolling direction. The specimens were subjected to various level of prestrain from 0% to 6% engineering strain. In addition, the plate specimens, as shown in Fig. 1, were machined by wire electrical discharged machining and then tensioned to the different prestrain level (0%, 1%, 2%, 3% and 4%). The hydrogen permeation samples (shaded area in Fig. 1) were cut from the gauge parts of prestrained plate specimens. Subsequently, all specimens were mechanically ground with SiC grinding paper up to 800 grit and rinsed with alcohol.

Some groups of prestrained specimens were electrochemically charged with hydrogen in 0.5 mol/L H₂SO₄ solution at various current densities ranging from 0.05 mA/cm² to 0.6 mA/cm² for 24 h at room temperature (298 K). The CH₄N₂S (1 g/L) was added in the solution as a hydrogen recombination poison. Platinum was used as an anode and the specimen was used as a cathode. To prevent hydrogen releasing from the charged specimens, cadmium electroplating was carried out immediately after hydrogen-charging, which was performed in an aqueous solution with 98% oil of vitriol (50 g/L), CdSO₄ powder (50 g/L), Na₂SO₄ (45 g/L), glutin (6 g/L) and phenol (3 g/L) at the current density of 25 mA/cm² for 5 min. The cadmium was used as an anode and the specimen was used as a cathode. Tensile tests were conducted on these prestrained and charged specimens at a crosshead speed 0.03 mm/min, corresponding to a normal strain rate of 2×10^{-5} /s. The prestrained specimens without hydrogen charging was also tensile tested as a reference. After tensile tests, the fracture surfaces of tensile specimens were observed by field emission scanning electron microscope (FESEM).

Another group of prestrained specimens were mechanically polished and etched in 4% Nital solution to observe the microstructure using an optical microscope. In addition, discs were cut from the some prestrained samples perpendicular to the axial direction. By mechanical thinning, the discs foils were created and further prepared by twin-jet electropolishing in a solution of 10% perchloric acid and 90% alcohol at 243 K. Through using JEM-200CX transmission electron microscopy (TEM), variation of dislocation structures at different prestrain was investigated.

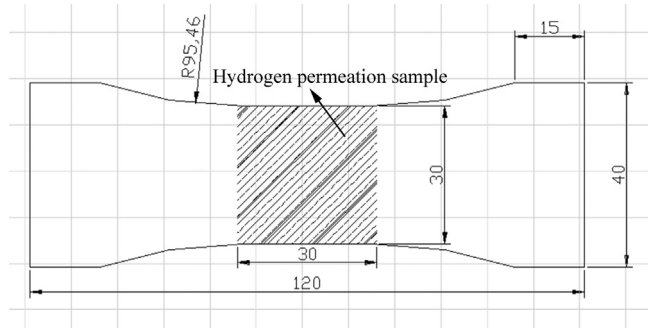


Fig. 1. Dimensions (in mm) of the plate specimen for hydrogen permeation tests. Note the thickness 1.5 mm.

3. Results

3.1. Hydrogen permeation tests

Electrochemical permeation technique originally developed by Devabathan and Stachurski was employed to study the hydrogen permeation behavior of prestrained steels [22]. The hydrogen permeation instrumentations were composed of an electrolytic cell with two compartments (cathodic and anodic sides), a reference electrode (Hg/HgO/NaOH 0.1 M NaOH), two auxiliary electrodes (Pt plate) and two potentiostat/galvanostat. The specimen with an exposed surface area of 2.27 cm² on each side was clamped between the compartments. One side of the specimen acted as hydrogen entry side. It was galvanostatically polarized at a constant charging current density (20 mA/cm²) in 0.5 M H₂SO₄ with 0.824 g/L Na₄P₂O₇. Prior to hydrogen charging, the specimens were depleted of residual hydrogen until the current lowered to 1.13 µA. The hydrogen exit side of the cell was potentiostatically maintained at a constant potential of -200 mV versus reference electrode. Fig. 2 shows the transient hydrogen permeation current density curves for various prestrain specimens.

We used the following equations to calculate permeability coefficient ($J_{\infty}L$) and effective hydrogen diffusivity (D_{eff}):

$$J_{\infty}L = \frac{I_p^{\infty}L}{nF} \quad (1)$$

$$D_{\text{eff}} = \frac{L^2}{6t_L} \quad (2)$$

In the equations listed above, I_p^{∞} (A/m²) was the steady-state permeation current density, n the number of electrons transferred, F (C/mol) the Faraday's constant, L (m) the specimen thickness, t_L (s) was the lag time, defined as 0.63 times the steady-state value. The experimental hydrogen permeability data of prestrained specimens are shown in Table 2. With an increase in prestrain, the diffusion coefficient of hydrogen decreases.

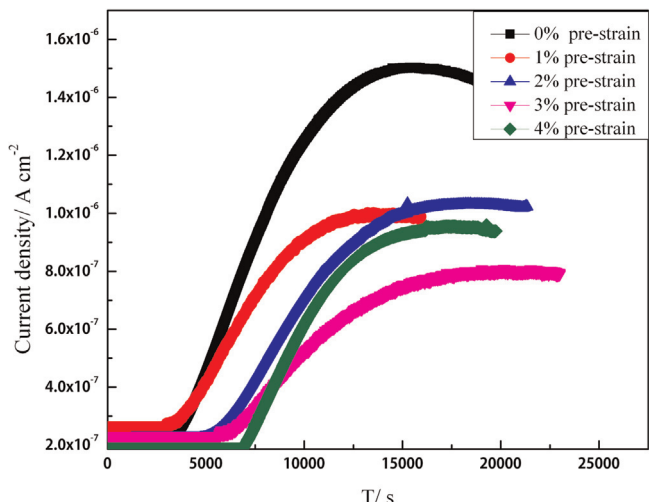


Fig. 2. The transient hydrogen permeation current density curves for various prestrain specimens.

Table 2

Experimental hydrogen permeability data as a function of different prestrain.

Prestrain (%)	Thickness (mm)	t_L (s)	$J_{\infty}L$ (mol/ms)	D_{eff} (m^2/s)
0	1.10	7748	1.712×10^{-10}	2.603×10^{-11}
1	1.02	6733	1.564×10^{-10}	2.575×10^{-11}
2	1.12	9391	1.194×10^{-10}	2.223×10^{-11}
3	1.10	9822	9.098×10^{-11}	2.053×10^{-11}
4	1.02	9887	9.110×10^{-11}	1.754×10^{-11}

3.2. Stress-strain curve

A typical stress-strain curve of the non-prestrained sample is presented in Fig. 3. The necking occurs when the uniform strain is more than 7.2%. The mechanical properties of the steel are given in Table 3.

3.3. Microstructure

The microstructures of both non-prestrained and prestrained specimens are shown in Fig. 4(a–c). The microstructures of 0%, 3% and 6% prestrained specimens have minor deviations. One can see that the microstructures consist of bainite and martensite. The spherical inclusions are observed to distribute randomly in the steel matrix, as shown in Fig. 4(d). Fig. 5 shows the close-up TEM images. The images reveal the higher number of dislocations in a specimen subjected to 6% prestrain compared with that in a specimen of 0% prestrain. One can observe tangled dislocation (indicated by black arrowhead) in the specimen of 6% prestrain, as shown in Fig. 5(b).

3.4. Tensile properties

Typical stress–displacement diagrams for hydrogen-uncharged and -charged at various current density prestrained specimens with 0%, 1%, 3%, 5% and 6% prestrain are shown in Fig. 6. For all hydrogen-uncharged specimens, the stress increases with the

Table 3

Mechanical properties of the non-prestrained steel.

YS (MPa)	UTS (MPa)	ψ (%)	δ (%)	Hardness (HRC)
1130	1300	60.5	15.9	46

YS: yield strength; UTS: ultimate tensile strength; ψ : reduction of area; δ : elongation at fracture.

displacement, reaches ultimate tensile strength (UTS), decreases with further displacement and then the fracture occurs, as shown in Fig. 6(a). However, the hydrogen-charged specimens show severe HE, they fracture prematurely in their elastic stage and without evident plastic deformation, as shown in Fig. 6(b–d). It was reported that the early fracture due to HE in 310 stainless steel [18] or ferrite/martensite dual-phase steel [23] occurred after a relatively high level of plastic strain. Therefore, compared to those steels, the high strength steels show much higher sensibility to HE. Fig. 7 shows the UTS or UTS-H at various current density specimens as a function of prestrain. At current density 0 and 0.05 mA/cm² shown in Fig. 7(a) and (b) respectively, the UTS or UTS-H increases with increasing prestrain while at higher current density 0.45 and 0.6 mA/cm², the UTS-H initially increases, reaches the peak value at 3% prestrain and then dramatically decreases, as shown in Fig. 7(c) and (d) respectively. Fig. 8 shows the UTS or UTS-H of various prestrain as a function of hydrogen charging current density. The UTS-H of the same prestrained specimens decreases with an increase in current density, especially for 6% prestrain.

3.5. Fractographic analysis

Fig. 9 shows the fracture surfaces of 3% prestrain specimen that is hydrogen-uncharged. Two distinct regions, corresponding to the crack initiation and propagation in the central region and the final unstable fracture in the peripheral region respectively, can be observed, as shown in Fig. 9(a). The crack initiates at the center of the specimen. High magnification observation, consisting of

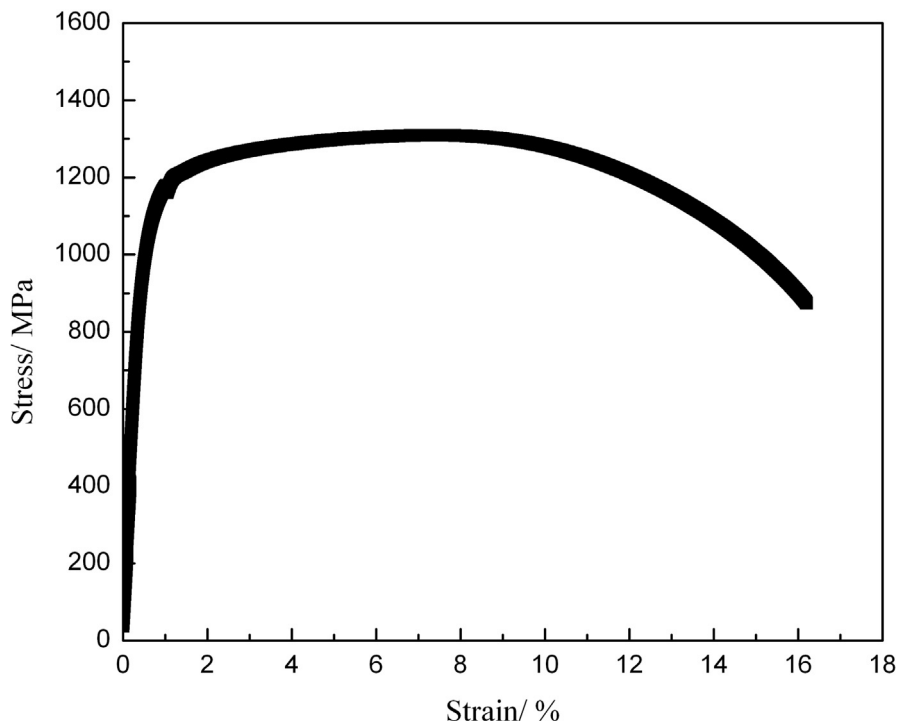


Fig. 3. Engineering stress–strain curve of the non-prestrained sample.

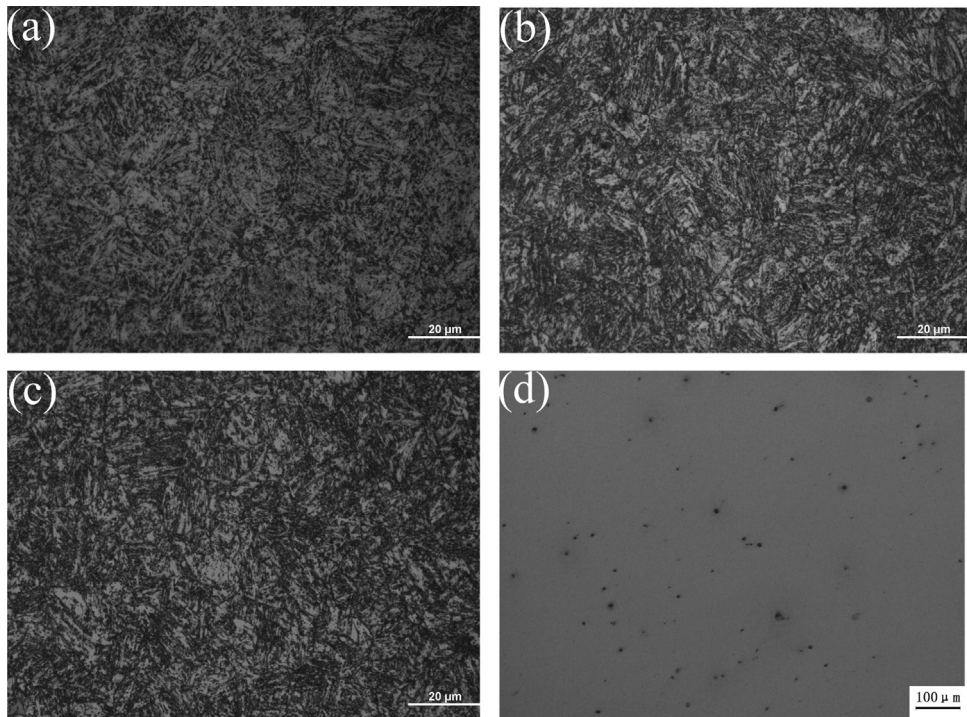


Fig. 4. Optical micrographs of (a) 0% prestrain; (b) 3% prestrain; (c) 6% prestrain; (d) inclusions contained in the steel.

dimples with a range of sizes, reveals a ductile fracture, as shown in Fig. 9(b). Unlike the crack initiation site, the propagation region comprises both small dimples and many secondary cracks, as shown in Fig. 9(c). The peripheral region is the shear lip, which is composed of finer dimples than those in crack initiation and propagation region, as shown in Fig. 9(d). Fig. 9(e) shows the mixed inclusion, containing Ca-Al-Si-O, in crack initiation region.

Fig. 10 shows the fracture surfaces of 3% prestrain specimen that is hydrogen-charged at the current density 0.45 mA/cm^2 . Like the hydrogen-uncharged specimen, the fracture surface also has two regions, the region of the crack initiation and propagation and the peripheral region of the shear lip in Fig. 10(a). The crack nucleation site is located at the inclusion. In addition, the hydrogen-charged specimen shows a brittle fracture. The crack initiation site exhibits a mixed fracture mode: quasi-cleavage fracture and intergranular fracture accompanied with secondary cracks (indicated by black arrowhead) and micropores (shown by white arrowhead) on the grain boundary, as shown in Fig. 10(b). They were typical characteristics of HE for high strength steel [4]. Compared with hydrogen-uncharged specimen in Fig. 9(c), the number of secondary cracks decline. The formation of secondary cracks can relax the stress concentration, absorb lots of energy and

reduce HE. The crack propagation region shows quasi-cleavage fracture with a little dimples, as shown in Fig. 10(c). Fig. 10(d) presents the EDAX analysis of the inclusion and the inclusion is also composed of Ca-Al-Si-O. Note that similar fracture fractographs are observed when hydrogen-charging current density is at 0.05 mA/cm^2 . Fig. 11(a) shows the macro-fracture appearance of 3% prestrain specimen that is hydrogen-charged at the current density 0.6 mA/cm^2 , also showing brittle fracture. High magnification images exhibit intergranular fracture, as shown in Fig. 11(b).

The relationship between the area fraction of intergranular fracture and hydrogen charging current density of 3% prestrain specimens is shown in Fig. 12. The area fraction of intergranular fracture increases as current density enhances.

4. Discussion

4.1. Effect of prestrain on hydrogen behavior

Hydrogen diffusion plays an important role in hydrogen induced crack. On the basis of trap activation energy, which affects the escape rate of hydrogen from trapping sites, traps are divided

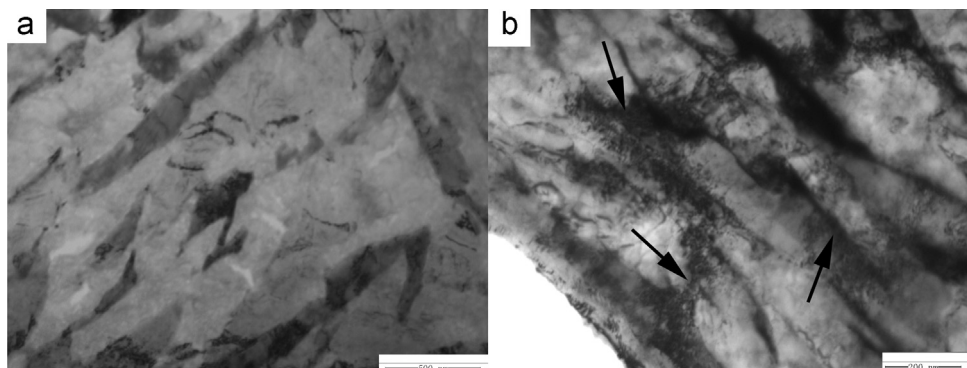


Fig. 5. TEM images of dislocations structures (a) 0% prestrain; (b) 6% prestrain, black arrowhead indicating tangled dislocation.

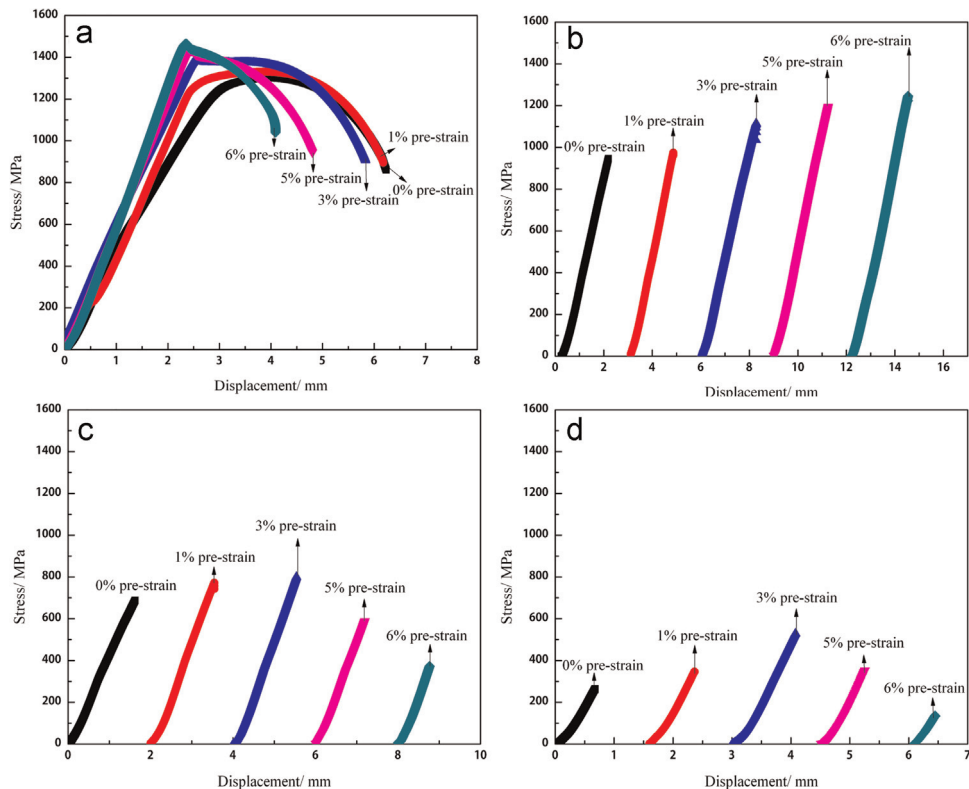


Fig. 6. Stress–displacement diagrams for hydrogen-uncharged and -charged at various hydrogen charging current density prestrained specimens with (a) 0 mA/cm²; (b) 0.05 mA/cm²; (c) 0.45 mA/cm² and (d) 0.6 mA/cm² for 24 h at room temperature (298 K).

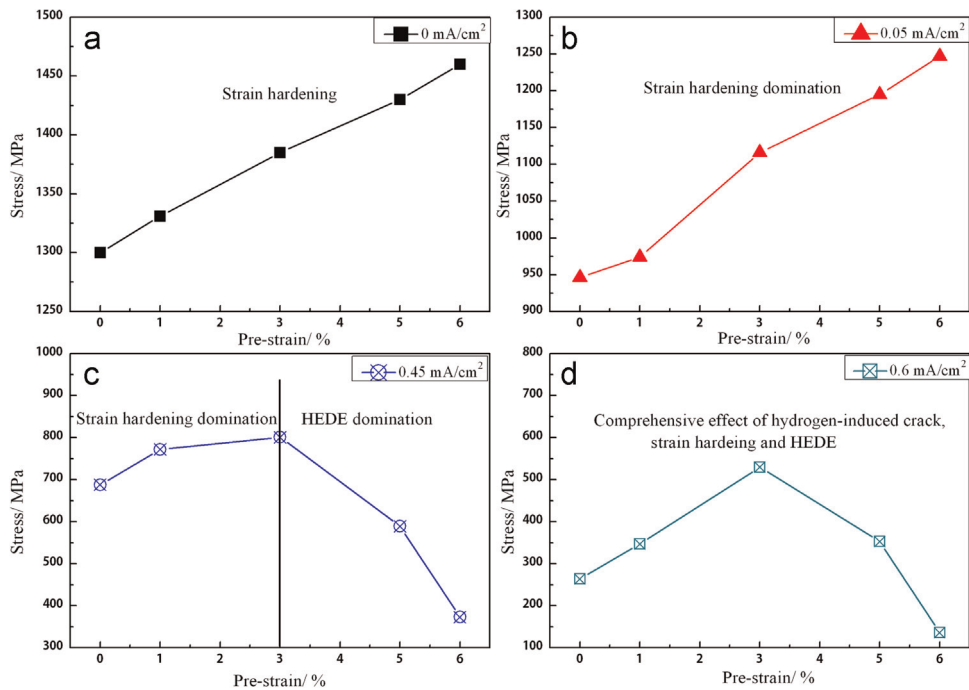


Fig. 7. UTS or UTS-H at different hydrogen charging current density as a function of prestrain. (a) 0 mA/cm²; (b) 0.05 mA/cm²; (c) 0.45 mA/cm² and (d) 0.6 mA/cm².

in irreversible traps with binding energy $W_B > 60$ KJ/mol and reversible traps with $W_B < 30$ KJ/mol. Interstitial sites, dislocations and grain boundaries etc. are referred as reversible traps while those for ferrite/cementite interfaces and various non-metallic inclusions such as Y_2O_3 , MnS, Al_2O_3 are regarded as irreversible traps. After prestrain, the dislocation density increases, corresponding to increase in hydrogen traps, and thus causes a decrease

in hydrogen diffusion. The results are consistent with the previous references [24,25].

4.2. Crack initiation, growth in hydrogen-uncharged and -charged prestrained specimens

In hydrogen-uncharged 3% prestrain specimens, the crack

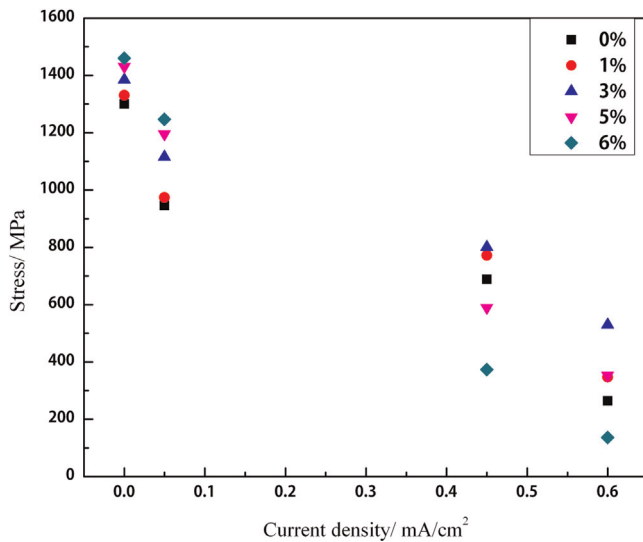


Fig. 8. UTS or UTS-H of various prestrain as a function of hydrogen charging current density.

initiation site is located at the central of the specimen. The fracture surface shows microvoid accumulation fracture. Some literature revealed that the mixed oxide inclusions were favorable for void nucleation [26,27].

Researchers [18,28,29] reported that HE of steels was related to diffusive hydrogen as it operated as a source for local hydrogen enrichment. In hydrogen-charged ($0.45 \text{ mA}/\text{cm}^2$) 3% prestrain specimen, the crack initiates at the Ca-Al-Si-O mixed inclusions, which serve as irreversible traps. After hydrogen charging, a distinct aggregation of hydrogen at the interface between matrix and inclusion was reported [30–32]. The inclusions enriched in Al oxide are hard, brittle and not cohesive to the matrix. In the case of tensile tests, the uncoordinated deformation between the matrix and inclusions results in a high local stress concentration at the interface. Hence, hydrogen atoms diffuse toward the interface drove by the stress gradient, causing larger local hydrogen concentration around stress concentration sites. Zhang et al. [33] and Wang et al. [34] revealed that an additional tensile stress could be introduced by hydrogen, and increased linearly with the increasing hydrogen concentration. When total stress containing external tensile stress and hydrogen-induced additional stress exceeds

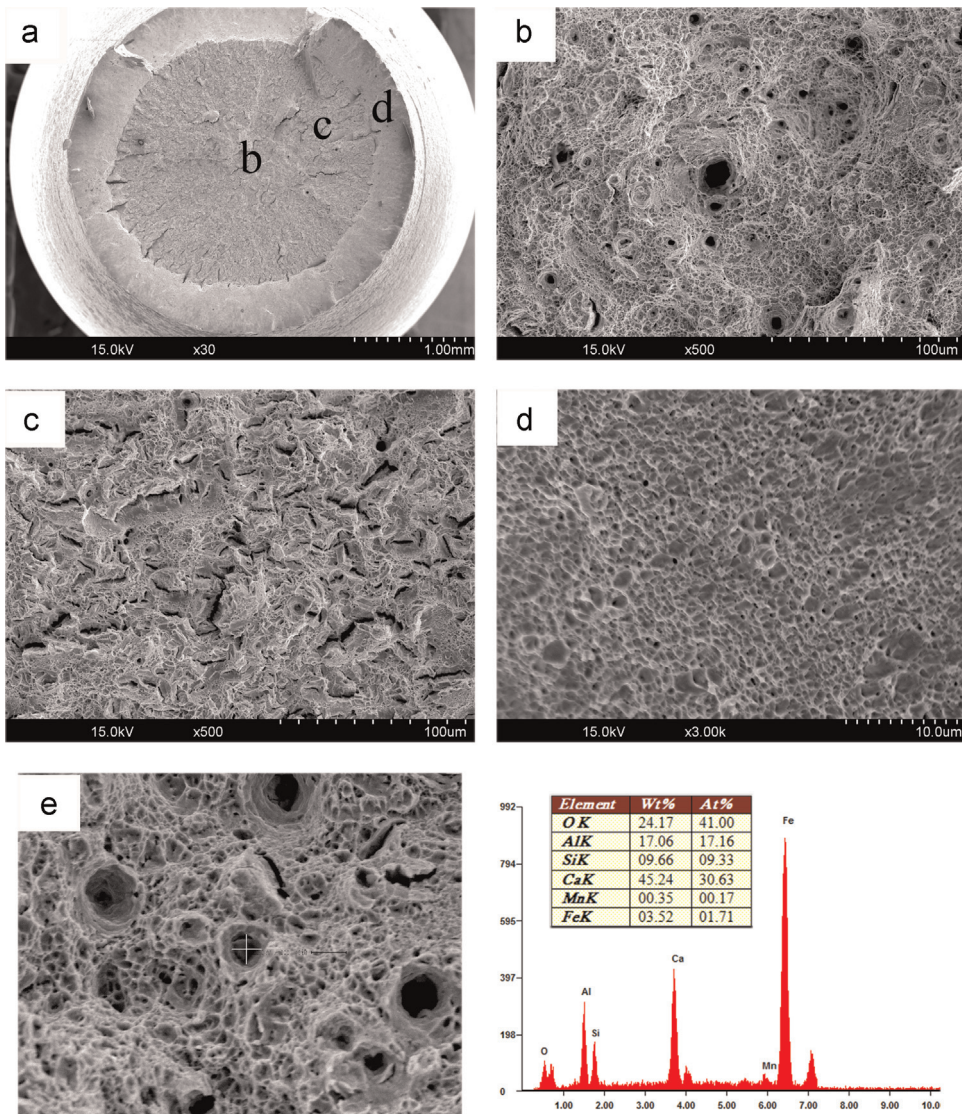


Fig. 9. SEM fractographs of hydrogen-uncharged specimens with 3% prestrain. (a) Overview of fracture surface; (b), (c) and (d) high magnification images of the signified region in image (a). (e) EDAX analysis of inclusions.

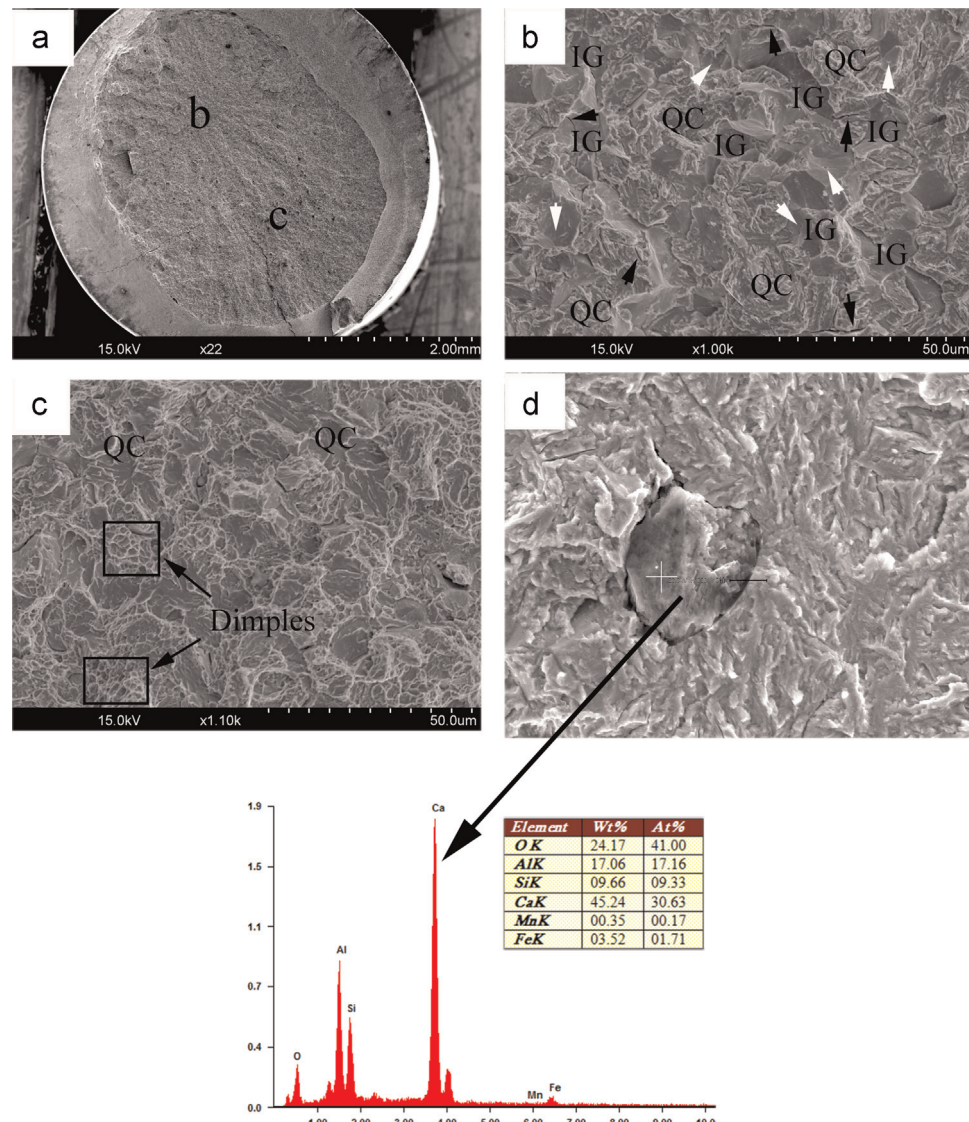


Fig. 10. SEM fractographs of hydrogen-charged specimens at current density $0.45 \text{ mA}/\text{cm}^2$ with 3% prestrain. (a) Overview of fracture surface; (b) and (c) high magnification images of the signified region in image(a); (d) EDAX analysis of inclusions at crack nucleation sites. Black arrowhead indicating secondary cracks and white arrowhead showing micropores. IG: intergranular fracture. QC: quasi-cleavage.

interface bonding force, the micro-crack forms.

The thermodynamic model [35], proposed by Rice–Wang, described that fracture mode of solids was determined by the competition between brittle interfacial cleavage separation and crack-tip blunting. Based on first-principle simulation, Yamaguchi et al.

[36] revealed that the cohesive energy was decreased 40 pct under the effect of immobile hydrogen. Taking the effect of mobile hydrogen into consideration, it was decreased by about 70–80 pct. In the presence of hydrogen, the reduction in cohesive strength of grain boundary could be greater than that of matrix. Thus, the

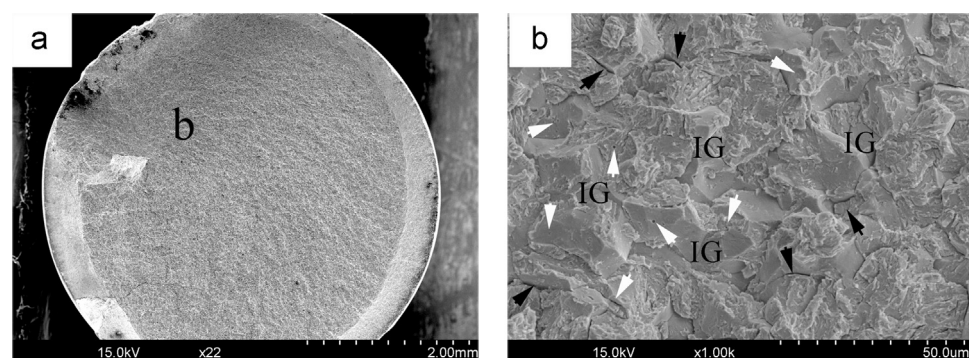


Fig. 11. SEM fractographs of hydrogen-charged specimens at current density $0.6 \text{ mA}/\text{cm}^2$ with 3% prestrain. (a) Overview of fracture surface; (b) high magnification images of the signified region in image (a). Black arrowhead indicating secondary cracks and white arrowhead showing micropores. IG: intergranular fracture.

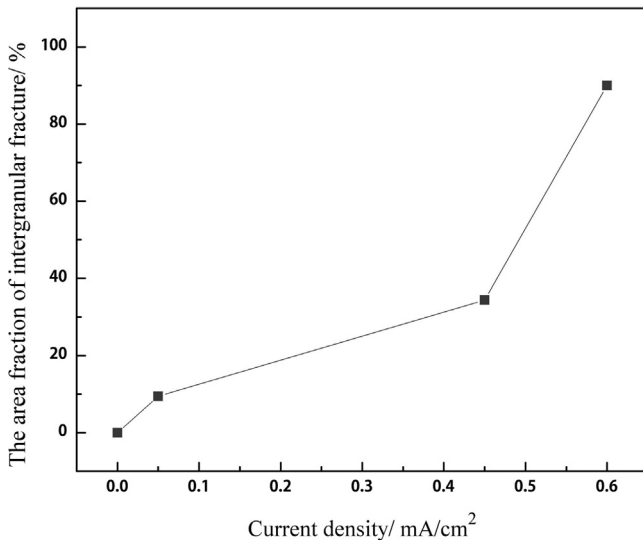


Fig. 12. The relationship between the area fraction of intergranular fracture and hydrogen charging current density in 3% prestrain specimens.

crack propagates along the grain boundaries and the crack initiation region exhibits intergranular fracture. When a critical value of stress at the rest area of the specimen is reached, the specimen fails.

Compared with the literature [34,37,38] that associated the hydrogen embrittlement with transgranular fracture, our results show intergranular cracking, as shown in Figs. 10(b) and 11(b). The fracture mode of hydrogen embrittlement is influenced by several factors such as hydrogen concentration, strength level, tensile rate and stress intensity factor, etc. The study [39] reported that intergranular fracture occurred when diffusible hydrogen content was 0.5 ppm for the strength level of 1050 MPa and less than 0.1 ppm for the strength level 1300 MPa. With increasing strength level, the hydrogen content of the onset of intergranular fracture decreased. Tsay et al. [37] revealed that the fractograph around the notch root showed quasi-cleavage at a tensile rate 1.25×10^{-4} mm/s while it exhibited intergranular fracture at a tensile rate 2.5×10^{-5} mm/s. This was due to that the hydrogen had sufficient time to accumulate at the crack tip at low tensile rate. In present study the hydrogen concentration [40] is much higher and the strain rate (2×10^{-5} /s) is much lower, and hydrogen is fully able to interact with grain boundaries, resulting in intergranular fracture.

4.3. The effect of hydrogen-charging current density on tensile properties

In hydrogen-uncharged specimens, the UTS increases with increasing the prestrain. This is most likely related to the increase in the densities of dislocations by the prestrain before the tensile tests, as shown in Fig. 5. This phenomenon has been well-known as strain hardening.

In present study, UTS-H decreases with an increase in current density under the same prestrain conditions, as shown in Fig. 8. The results are in accordance with the findings of Enos et al. [41] and Wang et al. [42,43] in non-prestrained specimens. Hydrogen Enhanced Decohesion (HEDE) is one of the earliest and most widely accepted HE mechanisms. It is an assumption that solute hydrogen reduces the atomic bonding force and the surface energy. According to the following equation [44]:

$$C_L = \frac{\varphi_0 N_a}{D_0} \exp\left(\frac{-8000}{RT}\right) \sqrt{i_c} \quad (3)$$

where φ_0 is permeation constant, D_0 is diffusion constant, and N_a is Avogadro constant. i_c is hydrogen charging current density. It can be seen that the hydrogen concentration C_L is proportional to $\sqrt{i_c}$. The higher current density, the higher hydrogen concentration. Hence the UTS-H decreases as current density increases. Hydrogen atoms tend to diffuse to the sites of crystalline defects, such as dislocations, grain boundaries. At 6% prestrain, tangled dislocations promote hydrogen enrichment and the local cohesive stress is inversely proportional to the accumulated hydrogen concentration. Thus, the loss of strength is the most serious in 6% prestrain, compared with other prestrain level.

When the current density is at 0.05 mA/cm², the tensile strength monotonously increases with an increase in prestrain, as shown in Fig. 7(b). This phenomenon is in good agreement with the results obtained in Refs. [17–19]. Unfortunately, the mechanism of this trend is not well-documented. On one hand, experimental results [29,40,45,46] and theoretical calculations [21] indicated that the quantity of hydrogen increased with increasing plastic strain. According to HEDE mechanism, the UTS-H should decrease as the prestrain increased. On the other hand, it is well-known that the dislocations density increases with increasing prestrain and the higher stress is needed, i.e. strain hardening. Therefore, UTS-H should increase. At current density 0.05 mA/cm², the content of hydrogen is low. The dislocations may disperse the hydrogen atom, reduce locally hydrogen enrichment and improve resistance of HE. In this case, the strain hardening dominates. So UTS-H gradually increases with increasing prestrain.

When the current density is at 0.45 mA/cm², the UTS-H firstly increases, reaches the peak value at 3% prestrain and then decreases, as shown in Fig. 7(c). This interesting phenomenon is interpreted by competition between strain hardening and HEDE mechanism. As mentioned above, the degree of HE is determined by local hydrogen concentration. At lower prestrain (0–3%), the uniform distribution dislocations reduce the local enrichment of hydrogen. Hence the strain hardening populations dominate, resulting in increasing UTS-H. In the case of higher prestrain (3–6%), HEDE mechanism populations prevail. The previous study [40] reported that the increase of hydrogen concentration was much remarkable at larger prestrain, as shown in Fig. 13. Because lots of hydrogen atoms enrich at tangled dislocations sites, the UTS-H

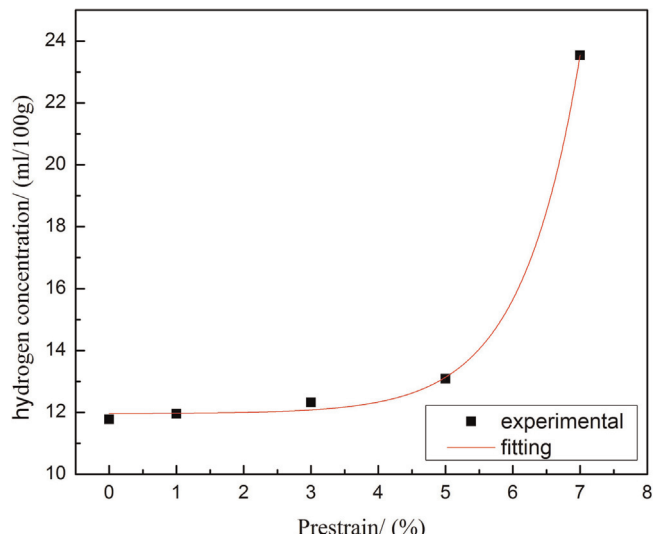


Fig. 13. The relationship between the hydrogen concentration and prestrain at current density 0.3 mA/cm² [40].

decreases at larger prestrain. However, the previous studies revealed that tensile strength of hydrogen-charged 310S stainless steels [18] and 2205 duplex stainless steels [19] increased with an increase in prestrain. This is attributed to lower diffusion coefficient and higher solubility of hydrogen in austenite phase of stainless steels in comparison with martensite steel. The strain hardening rather than HEDE mechanism dominates.

When the current density is at 0.6 mA/cm², the variation trend between UTS-H and prestrain is similar to that of 0.45 mA/cm², as shown in Fig. 7(d). But their failure mechanisms are quite different. Kim et al. [47] and Jin et al. [48] found that when the applied current density was over a certain value, the hydrogen-induced crack occurred and the crack was nucleated at the inclusions in the absence of external stress. The hydrogen atoms trapped at interface and exerted hydrogen pressure by formation of hydrogen molecules. When hydrogen pressure exceeded interface bonding force, the hydrogen-induced crack initiated. In order to prove whether hydrogen-induced crack was generated or not, the tensile tests were conducted on 3% prestrain specimens at current density 0.45 and 0.6 mA/cm², which were atmospherically discharged for ten days. The results show that the restrained specimen at 0.45 mA/cm² recovers its initial strength after ten days while tensile strength is 1120 MPa for 0.6 mA/cm² prestrained specimen. Due to the comprehensive effect of hydrogen-induced crack, strain hardening and HEDE, the UTS-H increases at first, reaches maximum value and then decreases.

5. Conclusions

The effect of hydrogen-charging current density on mechanical properties of prestrained high strength steels was investigated. The conclusions are as follows:

- (1) The relationship between UTS-H and prestrain depends on cathodic hydrogen-charging current density. At low current density, i.e. 0.05 mA/cm², the UTS-H monotonously increases with increasing prestrain as the strain hardening effect dominates in this case. However, at current density 0.45 mA/cm², the UTS-H firstly increases and then decreases with an increase in prestrain due to the competition between strain hardening and HEDE mechanism. The variation trend between UTS-H and prestrain at current density 0.60 mA/cm² is similar to that of current density 0.45 mA/cm². This is attributed to comprehensive effect of hydrogen-induced crack, strain hardening and HEDE mechanism.
- (2) Under the same prestrain conditions, the UTS-H decreases with increasing hydrogen-charging current density, especially for 6% prestrain.
- (3) Hydrogen diffusion coefficient gradually decreases as the prestrain increases. This is attributed to increasing dislocations, which can act as hydrogen traps.
- (4) In comparison to hydrogen-uncharged specimen, hydrogen charging causes a change from ductile failure to brittle mixed intergranular and quasi-cleavage failure. With increasing hydrogen charging current density, the area fraction of intergranular fracture increases in 3% prestrain specimens.

Acknowledgments

This research was financially supported by the Doctoral Research Assistant Foundation of Xi'an Jiaotong University.

References

- [1] A. Valiente, M. Elices, Eng. Fail. Anal. 5 (1998) 219–227.
- [2] J. Woodtli, R. Kieselbach, Eng. Fail. Anal. 7 (2000) 427–450.
- [3] X. Li, J. Zhang, P. Zhang, P. Li, X. Song, Journal of Failure Analysis and Prevention, 15(2), 2015, 295–299.
- [4] J.S. Kim, Y.H. Lee, D.L. Lee, K.-T. Park, C.S. Lee, Mater. Sci. Eng.: A 505 (2009) 105–110.
- [5] M. Wang, E. Akiyama, K. Tsuzaki, Corros. Sci. 49 (2007) 4081–4097.
- [6] T. Tabata, H. Birnbaum, Scr. Metall. 18 (1984) 231–236.
- [7] I. Robertson, H. Birnbaum, Acta Metall. 34 (1986) 353–366.
- [8] E. Sirois, H. Birnbaum, Acta Metall. Mater. 40 (1992) 1377–1385.
- [9] R. Kirchheim, Acta Mater. 55 (2007) 5139–5148.
- [10] A. Atrens, N. Fiore, K. Miura, J. Appl. Phys. 48 (1977) 4247–4251.
- [11] W. Xie, X. Liu, W. Chen, H. Zhang, Comput. Mater. Sci. 50 (2011) 3397–3402.
- [12] I. Robertson, Eng. Fract. Mech. 68 (2001) 671–692.
- [13] H. Matsui, H. Kimura, S. Moriya, Mater. Sci. Eng. 40 (1979) 207–216.
- [14] I.Y. Telitchev, O. Vinogradov, Comput. Mater. Sci. 36 (2006) 272–280.
- [15] W. Hofmann, W. Rauls, Weld. J. 44 (1965) S225–S230.
- [16] R. Walter, W. Chandler, Rocketdyne, North American Rockwell, Canoga Park, California, USA, 1969.
- [17] R. Davies, Metall. Trans. A 12 (1981) 1667–1672.
- [18] H. Ji, I.-J. Park, S.-M. Lee, Y.-K. Lee, J. Alloys Compd. 598 (2014) 205–212.
- [19] S. Chen, T. Wu, J. Wu, J. Mater. Sci. 39 (2004) 67–71.
- [20] Y. Wang, X. Wang, J. Gong, L. Shen, W. Dong, Int. J. Hydrog. Energy 39 (25) (2014) 13909–13918.
- [21] S. Wang, S. Ohnuki, N. Hashimoto, K. Chiba, Mater. Sci. Eng.: A 560 (2013) 332–338.
- [22] M. Devanathan, Z. Stachurski, Proc. R. Soc. Lond. Ser. A: Math. Phys. Sci. 270 (1962) 90–102.
- [23] M. Koyama, C.C. Tasan, E. Akiyama, K. Tsuzaki, D. Raabe, Acta Mater. 70 (2014) 174–187.
- [24] P.C. Rivera, V. Ramunni, P. Bruzzoni, Corros. Sci. 54 (2012) 106–118.
- [25] U. Bhat, H. Lloyd, J. Iron Steel Inst. 165 (1950) 382–389.
- [26] R.W. Staehle, Stress Corrosion Cracking and Hydrogen Embrittlement of Iron Base Alloys, June 12–16, 1973, National Association of Corrosion Engineers, Unieux, Firminy, France, 1977.
- [27] I. French, P. Weinrich, C. Weaver, Acta Metall. 21 (1973) 1045–1049.
- [28] D. Li, R.P. Gangloff, J.R. Scully, Metall. Mater. Trans. A 35 (2004) 849–864.
- [29] M. Nagumo, M. Nakamura, K. Takai, Metall. Mater. Trans. A 32 (2001) 339–347.
- [30] J. Ovejero-García, J. Mater. Sci. 20 (1985) 2623–2629.
- [31] K. Horikawa, N. Ando, H. Kobayashi, W. Urushihara, Mater. Sci. Eng.: A 534 (2012) 495–503.
- [32] M. Au, Mater. Sci. Eng.: A 454 (2007) 564–569.
- [33] T. Zhang, W. Chu, K. Gao, L. Qiao, Mater. Sci. Eng.: A 347 (2003) 291–299.
- [34] R. Wang, Corros. Sci. 51 (2009) 2803–2810.
- [35] J.R. Rice, J.-S. Wang, Mater. Sci. Eng.: A 107 (1989) 23–40.
- [36] M. Yamaguchi, K.-I. Ebihara, M. Itakura, T. Kadoyoshi, T. Suzudo, H. Kaburaki, Metall. Mater. Trans. A 42 (2011) 330–339.
- [37] L. Tsay, Y. Hu, C. Chen, Corros. Sci. 47 (2005) 965–976.
- [38] C. Beachem, Metall. Trans. 3 (1972) 441–455.
- [39] M. Wang, E. Akiyama, K. Tsuzaki, Scr. Mater. 52 (2005) 403–408.
- [40] X. Li, Y. Wang, P. Zhang, B. Li, X. Song, J. Chen, Mater. Sci. Eng.: A 616 (2014) 116–122.
- [41] D. Enos, J. Scully, Metall. Mater. Trans. A 33 (2002) 1151–1166.
- [42] M. Wang, E. Akiyama, K. Tsuzaki, Mater. Sci. Eng.: A 398 (2005) 37–46.
- [43] M.-Q. Wang, E. Akiyama, K. Tsuzaki, Mater. Sci. Technol. 22 (2006) 167–172.
- [44] J.K. Wu, Int. J. Hydrog. Energy 17 (1992) 917–921.
- [45] M. Nagumo, K. Ohta, H. Saitoh, Scr. Mater. 40 (1999) 313–319.
- [46] M. Nagumo, K. Takai, N. Okuda, J. Alloys Compd. 293 (1999) 310–316.
- [47] W.K. Kim, S.U. Koh, B.Y. Yang, K.Y. Kim, Corros. Sci. 50 (2008) 3336–3342.
- [48] T. Jin, Z. Liu, Y. Cheng, Int. J. Hydrog. Energy 35 (2010) 8014–8021.